Impact of reduced graphene oxide on the ethanol sensing performance of hollow SnO$_2$ nanoparticles under humid atmosphere

Cecilia A. Zito, Tarcísio M. Perfecto, Diogo P. Volanti *

LabMatSus—Laboratory of Materials for Sustainability, IBILCE, UNESP—Univ Estadual Paulista, Rua Cristóvão Colombo, 2265, S. J. Rio Preto, 15054-000, Brazil

ABSTRACT

The interference of humidity is a key factor to be considered in metal oxide semiconductors gas sensing performance. However, an efficient gas detection under humid conditions is a challenge. Herein, we report the effect of reduced graphene oxide (RGO) on volatile organic compounds (VOCs) sensing performance of hollow SnO$_2$ nanoparticles (NPs) under wet atmosphere. For this purpose, RGO-SnO$_2$ nanocomposite was obtained by a one-pot microwave-assisted solvothermal synthesis. The sensing tests for VOCs were conducted under dry air and at a relative humidity (RH) between 24 and 98%. The samples exhibited better response toward ethanol than to other VOCs such as acetone, benzene, methanol, m-xylene, and toluene, at the optimum operating temperature of 300 °C. Furthermore, RGO-SnO$_2$ nanocomposite showed an enhanced ethanol response in comparison with pure hollow SnO$_2$ NPs. Even under 98% of RH, the RGO-SnO$_2$ nanocomposite showed a response of 43.0 toward 100 ppm of ethanol with a response time of 8 s. The excellent sensor performance is related to the hollow structure of SnO$_2$ NPs, and the heterojunction between RGO and SnO$_2$. Therefore, the RGO content can be a promising approach to minimize the humidity effect on SnO$_2$ ethanol sensing performance.

© 2017 Elsevier B.V. All rights reserved.

1. Introduction

The detection of volatile organic compounds (VOCs) has attracted considerable attention due to its application in environmental and indoor air quality monitoring, as well as in non-invasive disease diagnosis [1,2]. For these purposes, gas sensors based on metal oxide semiconductors (MOS) are widely used because of their sensibility, low cost, and possibility of scaled-up production [3,4]. Among the MOS, SnO$_2$, an n-type semiconductor, is one of the most studied material for VOCs monitoring with a great sensitivity toward several gases, including acetone [5,6], formaldehyde [7,8], toluene [9], ethanol [10,11], methanol [12], and so on.

Composites of SnO$_2$ have shown to be a way to improve the sensing performance toward VOCs, for instance, composites with other MOS [13,14], noble metals [15,16], and graphene-based materials [2,17], are reported. The use of reduced graphene oxide (RGO), which is a p-type material, can enhance parameters such as sensor response, recovery rate, stability, sensitivity [17–19], and selectivity [20–22], because RGO enhances the electron transport [2] and provides more sites for gas molecules adsorption due to its large specific surface area, defects, sp^2-bonded carbon, and residual oxygenated functional groups [22–24].

For the real application of SnO$_2$ as a gas sensor, it is necessary to consider the influence of humidity since atmospheric air and exhaled breath contain a considerable quantity of water vapor [25,26]. However, the sensors based on MOS are much sensitive to humidity and, consequently, the response toward an analyte gas significantly decreases under wet conditions [27–30]. Thus, it is of great importance to developing sensors with less negative effect of humidity for actual applications. Some studies have demonstrated that Ti [31], or Sb-doping [32], and Pd-loading [28,33], can be effective ways to preserve the stability of the SnO$_2$ gas sensing performance. Nevertheless, to the best of our knowledge, few studies have been conducted to verify the effect of a little amount of RGO on the VOCs detection of SnO$_2$ NPs under controlled humid atmosphere.

In this study, we report a facile one-pot microwave-assisted solvothermal (MAS) synthesis of hollow SnO$_2$ NPs and RGO-SnO$_2$ nanocomposite. The phase composition, morphology, and physical-chemical properties were evaluated, and the first nucleation mechanism of SnO$_2$ was discussed involving olation and oxolation reactions. The obtained samples were tested as VOCs sensors in dry and humid atmosphere with a relative humidity (RH) between 24 and 98%. The findings demonstrated an enhanced

* Corresponding author.
E-mail address: volanti@ibilce.unesp.br (D.P. Volanti).

ethanol response for the RGO-SnO$_2$ nanocomposite compared with pure hollow SnO$_2$ NPs, which even at a RH of 98% exhibited a high response to 100 ppm of ethanol equal to 43.0.

2. Material and methods

2.1. Synthesis of RGO-SnO$_2$ nanocomposite

Graphite oxide (GO) was used as a precursor of reduced graphene oxide (RGO), and it was prepared by a modified Hummers' method as described in a previous report [34,35]. RGO-SnO$_2$ nanocomposite was synthesized by a one-step microwave-assisted solvothermal (MAS) method based on previously reported synthesis [36]. In a typical procedure, a 9.8 mg of GO was dispersed in 30 mL of deionized water (Millipore, 18.2 MΩ cm) using an ultrasonic bath for one hour to promote GO exfoliation. Afterward, 1.1973 g (4 mmol) of K$_2$SnO$_3$·3H$_2$O (Sigma-Aldrich, 99.9%) was added to 30 mL of ethylene glycol (Sigma-Aldrich, 99%), subsequently to the addition of 1.1976 g (19.9 mmol) of urea (Sigma-Aldrich, 99%). The solution containing the tin precursor was mixed with GO dispersion, and it was maintained under magnetic stirring for 10 min. After the stirring, the final mixture was transferred to a polytetrafluoroethylene (PTFE) autoclave, sealed and heated at 140 °C for 1 h in a microwave system (2.45 GHz/800W) [37]. After the heating, the autoclave was naturally cooled to room temperature. The products were collected by centrifugation, and washed several times with deionized water and ethanol, then dried at 80 °C. The RGO-SnO$_2$ nanocomposite with a RGO load of 2% (m$_{GO}$/m$_{Sn(IV)}$) was synthesized because this ratio showed to be the most promising for VOCs sensing performance. The synthesis of pure SnO$_2$ was carried out by the same method without GO addition.

2.2. Material characterizations

X-ray diffraction (XRD) characterization was performed using a Rigaku MiniFlex 300 powder diffractometer, with the Cu Kα radiation (λ = 1.54059 Å), operated at 30 kV and 10 mA in steps of 0.1°. The samples were scanned in the 2θ range of 5 and 80° at a scan rate of 1° min^{-1}. Raman spectra were measured using a HORIBA T64000 triple grating spectrometer with a laser excitation of 633 nm. Fourier transformed infrared (FTIR) spectra were recorded on a Perkin Elmer spectrophotometer Spectrum Two fitted with ATR device, in the range of 450–4,000 cm^{-1}. The morphology was analyzed with a field-emission transmission microscope (TEM, FEI Tecnai G^2 F20) and transmission electron microscope (TEM, Philips model CM200), both operated at an accelerating voltage of 200 kV. The thermogravimetric analysis (TG) was performed in a Perkin–Elmer TGA-4000 thermogravimetric balance in air atmosphere, at a scanning rate of 15 °C min^{-1}. Specific surface area was determined by Brunauer–Emmett–Teller (BET) method by nitrogen physisorption using a Gemini VII – Surface Area and Porosity analyzer. X-ray photoelectron spectroscopy (XPS) was performed in a K-Alpha Thermo Scientific spectrometer, using Al Kα radiation (1486 keV). The XPS spectra were calibrated with reference to the C 1 s peak (284.8 eV).

2.3. Gas sensor fabrication and measurement

The VOCs sensors were prepared by dispersing 7 mg of the powders in 2 mL of isopropanol using ultrasonication for 10 min. Alumina substrates with gold arrays as interdigitated electrodes on their surface were coated with the dispersion of samples powders. Then, the substrates were heated at 200 °C for 1 h 20 min under air atmosphere in order to stabilize the sensor and elimi-
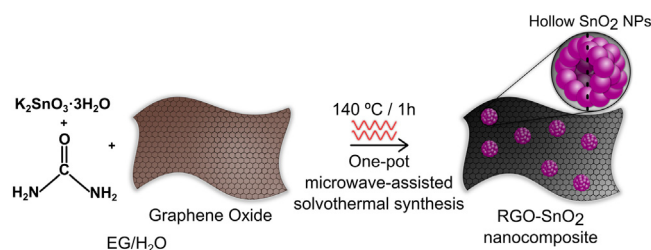

Fig. 1. Schematic illustration of the formation of RGO-SnO$_2$ nanocomposite by a one-pot microwave-assisted solvothermal synthesis.
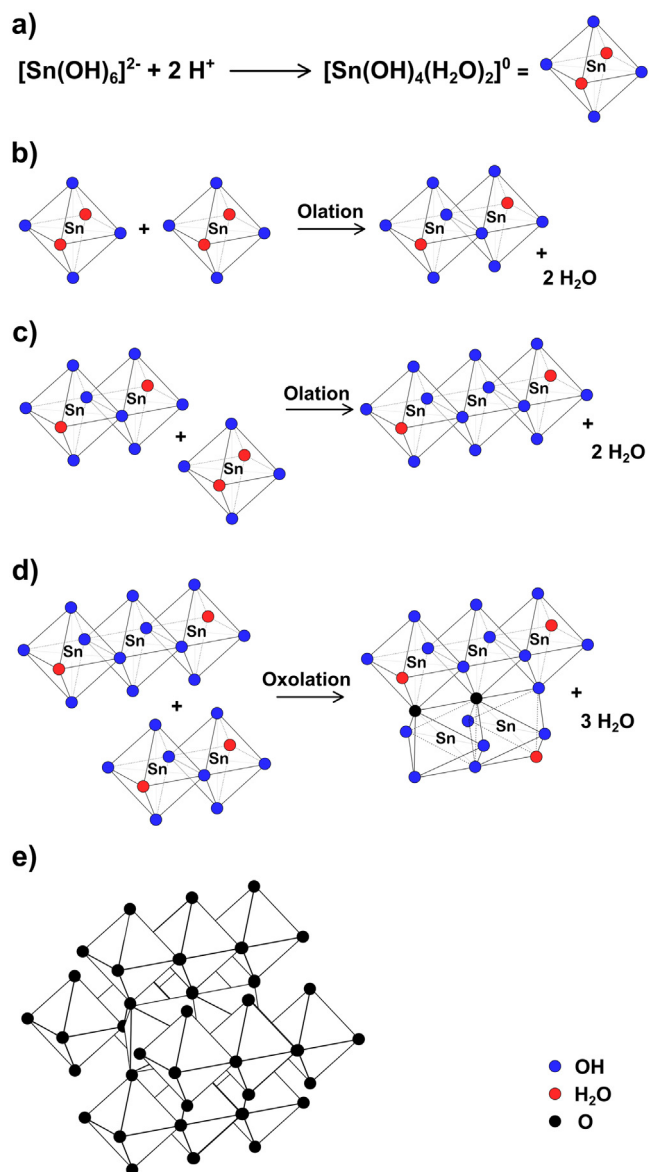
nate the isopropanol. The gas sensing performance was evaluated by exposing the sensors toward the VOCs and analyzing the change in electrical resistance. To measure the resistance change, a high-voltage source-measure unit (Keithley Source meter 2400) was used, applying a voltage of 5 V. The gas sensing properties were studied by exposing the sensor to the VOCs in the concentration range of 5–500 ppm, where six different gases were studied including acetone, benzene, ethanol, methanol, m-xylene, and toluene. The sensors were allocated inside the test chamber and heated at the studied temperature (100–400 °C) under air flow of 250 mL min^{-1}. At the desired temperature, the air flow was stopped and the chamber was closed until stabilizing the resistances. After obtaining the baseline, the required amount of VOCs was inserted in the test chamber using a syringe, and the exposure time was established as 100 s. After this time, an air flow of 250 mL min^{-1} was used to clean the system from the VOCs and to return to the baseline. The same procedure was carried out to study the humidity influence on the gas sensing performance. The VOCs sensing studies were conducted at the optimum operating temperature under four different relative humidity (RH) (24, 43, 73, and 98%), which was measured by using a thermohygrometer (HANNA, HI9564 model). In order to control the RH, the air flow passed through a closed vessel containing saturated solutions of some salts before entering the test chamber. Thus, the RH inside the test chamber was controlled at 24, 43, 73, and 98% by using saturated solutions of CH$_3$CO$_2$K, K$_2$CO$_3$, NaCl, and K$_2$SO$_4$ [38], respectively. The VOCs response was defined as the ratio of the resistances R$_{air}$/R$_{gas}$, where R$_a$ is the resistance in air (dry or humid) and R$_g$ is the resistance after exposing to the VOCs.

3. Results and discussion

3.1. Synthesis and crystal growth

RGO-SnO$_2$ nanocomposite was synthesized by a facile one-pot MAS method, as illustrated in Fig. 1. K$_2$SnO$_3$·3H$_2$O, urea, and GO dispersion were used as precursors in a reaction medium of water and ethylene glycol (EG). The microwave heating at 140 °C for 1 h promoted the formation of hollow SnO$_2$ nanoparticles in a spherical shape (Supplementary information – Fig. S1) concomitantly to GO reduction to RGO. The hollow SnO$_2$ NPs grow in the same way with or without GO in the reaction medium, however in the case of the nanocomposite, GO sheets act as support for SnO$_2$ growth.

The formation of SnO$_2$, using potassium stannate and urea as precursors, can be explained by olation and oxolation reactions (Fig. 2). In an alkaline medium, Sn(IV) is found as its monomeric hydroxide form of [Sn(OH)$_6$]$^{2-}$ ions. The thermohydrolysis of urea releases CO$_3$$^{2-}$ in the reaction medium, liberating H$^+$ ions. Such acidification results in the appearance of aquo ligands in the coordination sphere of Sn(IV), forming the zero-charge complex [Sn(OH)$_4$(H$_2$O)$_2$]^0, as shown in Fig. 2a. The initial step of condensation of [Sn(OH)$_4$(H$_2$O)$_2$]^0 proceeds by olation reaction, where both octahedra share an edge to form the dimer [Sn$_2$(OH)$_6$(μ-

a)

$[Sn(OH)_6]^{2-} + 2\,H^+ \longrightarrow [Sn(OH)_4(H_2O)_2]^0 =$

b)

Olation

$+\ 2\,H_2O$

c)

Olation

$+\ 2\,H_2O$

d)

Oxolation

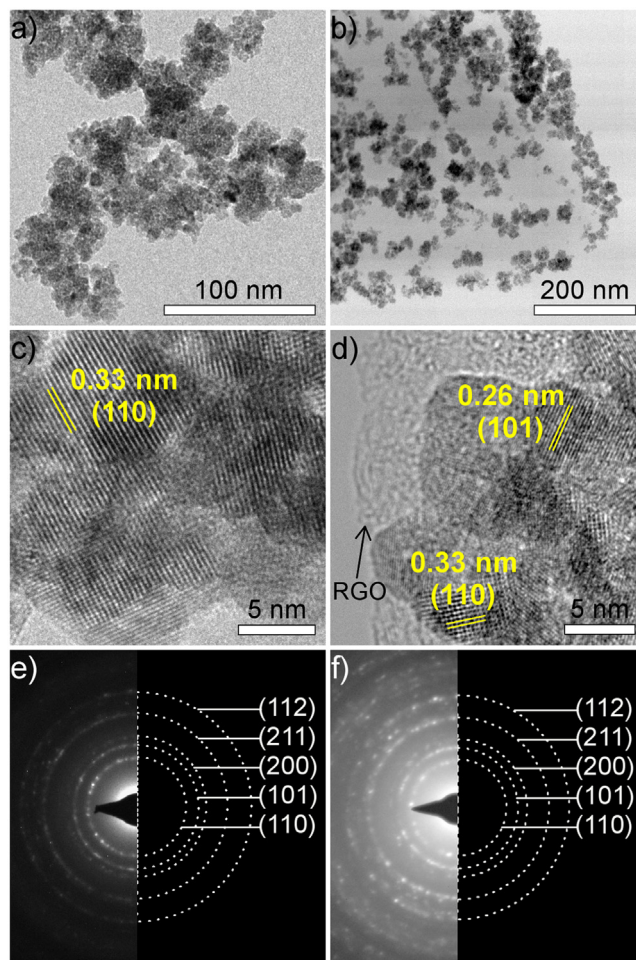$+\ 3\,H_2O$

e)

- ● OH
- ● H_2O
- ● O

Fig. 2. Process of SnO_2 formation by olation and oxolation. (a) acidification pro-
moted by urea leading to the formation of the zero-charge complex; (b) olation
reaction between two zero-charge complex, obtaining the dimer; (c) condensa-
tion by olation reaction between dimer and monomer; (d) condensation process
by oxolation; (e) final rutile-type structure of SnO_2.

$OH)_2(H_2O)_2]$ (Fig. 2b). Then, the condensation continues by olation
reaction between this dimer and monomer, in which the edge shar-
ing occurs in the same plane that the previous reaction, forming a
straight chain in the trimer $[Sn_3(OH)_8(\mu\text{-}OH)_4(H_2O)_2]$ as shown in
Fig. 2c [39,40]. Due to the presence of few aquo ligands, the oxola-
tion (formation of oxo bridge by water elimination) takes place in
the condensation process from now on [40] (Fig. 2d). The condensa-
tion by oxolation leads to the rutile-type crystal structure of SnO_2,
in which SnO_6 octahedra share edges and corners as illustrated in
Fig. 2e.

3.2. Morphological and structural characterization

The morphology of the samples was characterized by TEM
(Fig. 3). The TEM image of pure SnO_2, shown in Fig. 3a, revealed
the formation of uniform nanospheres composed of NPs in size
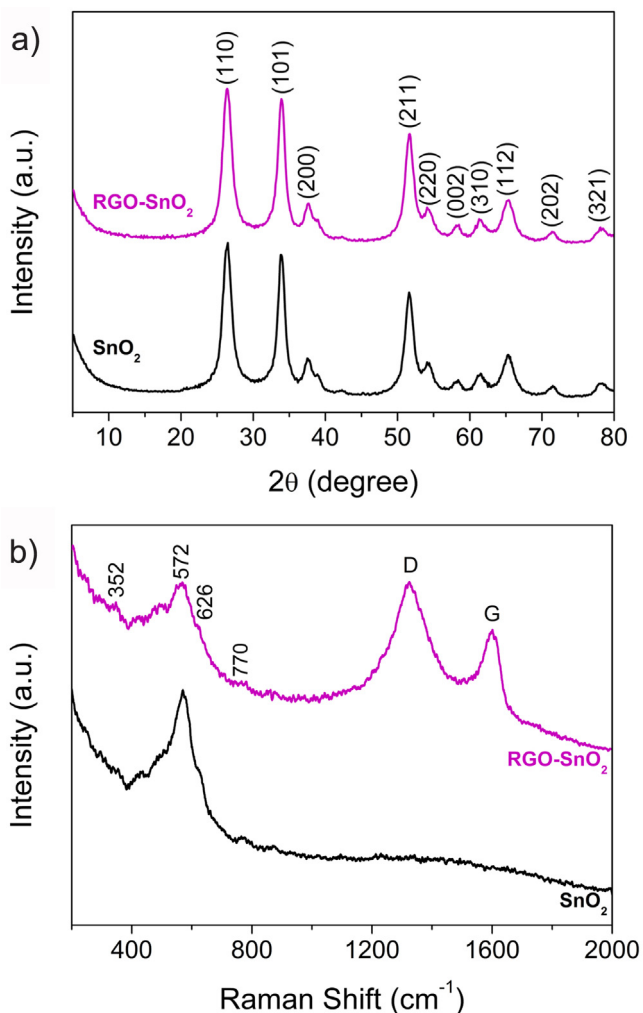range of 6–10 nm, as well as the hollow nature of the material,

Fig. 3. TEM images of (a) pure SnO_2 NPs, (b) RGO-SnO_2 nanocomposite. High-
resolution TEM (HRTEM) of (c) pure SnO_2 NPs, (d) RGO-SnO_2. Selected area electron
diffraction (SAED) patterns of (e) SnO_2, (f) RGO-SnO_2.

which was elucidated by the contrast between the light center and
dark boundary. This form of arrangement of the NPs results in a
porous structure. Fig. 3b contains the TEM image of the RGO-SnO_2
nanocomposite. The spherical morphology of hollow SnO_2 NPs was
preserved; however, it can be seen that SnO_2 NPs grew on the sur-
face of RGO sheets, which ensure a great interconnectivity between
SnO_2 and RGO.

By high-resolution TEM (HRTEM) image of pure SnO_2 (Fig. 3c),
the (110) crystal plane of tetragonal SnO_2 could be indexed, cor-
responding to an interplanar distance of 0.33 nm. HRTEM image
of the RGO-SnO_2 nanocomposite revealed the RGO content in the
nanocomposites structures, as shown in Fig. 3d. Moreover, HRTEM
image of RGO-SnO_2 reveals the inter-planar distance of 0.33 nm,
related to the (110) plane, as well as the inter-planar distance of
0.26 nm corresponding to the (101) plane. The selected area elec-
tron diffraction (SAED) patterns of pure SnO_2 NPs and RGO-SnO_2
are shown in Fig. 3e and f, respectively. The diffraction rings could
be indexed to tetragonal rutile SnO_2, exhibiting the (110), (101),
(200), (211) and (112) planes.

XRD was carried out for crystal structure investigation, and the
XRD patterns of pure SnO_2 NPs and RGO-SnO_2 nanocomposite are
shown in Fig. 4a. For both samples, the diffraction peaks could be
indexed to the tetragonal rutile structure of SnO_2 with $P4_2/mnm$
(136) space group (JCPDS no. 41–1445). No secondary peaks were
observed. The crystallite size calculated along the (110) plane by

Fig. 4. (a) XRD patterns and (b) Raman spectra of SnO$_2$ NPs and RGO-SnO$_2$ nanocomposite.

The BET specific surface area of the RGO-SnO$_2$ nanocomposite was 131 m^2 g^{-1}. This increase in the surface area indicated the interaction between SnO$_2$ NPs and RGO sheets, which may improve the VOCs sensing properties.

FTIR spectroscopy was employed to examine the chemical composition of the samples. The FTIR spectra of the samples are shown in Fig. S3, in which the same absorptions peaks are noticed. In the SnO$_2$ spectrum, the strong peak at 500 cm^{-1} was assigned to the antisymmetric vibration of O−Sn−O, whereas in the nanocomposite spectrum such peak is at around 511 cm^{-1}. The absorption peak at 606 cm^{-1} was due to the stretching vibration of Sn−O [47]. Another characteristic peak was observed at 1,650 cm^{-1} related to the bending vibrations of O−H from absorbed water molecules. The presence of water could be further confirmed by the absorption band at 3,293 cm^{-1} which corresponds to the stretching vibrations of O−H from adsorbed water, free or bonded [11]. However, in the nanocomposite spectrum, a decrease in the intensity of such peak was observed, which suggests that fewer water molecules adsorb on the material due to RGO presence.

Fig. S4 shows the TG curves of pure SnO$_2$ NPs and RGO-SnO$_2$ nanocomposite under air atmosphere. As shown in TG curve of SnO$_2$ (black curve), two weight loss steps were observed. The first step from 70 to 220 °C corresponded to a loss of 6.5%, being attributed to the removal of physically adsorbed water on the SnO$_2$ particles [48,49]. The second step lost 5.5% occurring up to 530 °C is assigned to the elimination of chemically bonded water [48,49], and ammonia as well [50], prevenient from urea. In the TG curve of the RGO-SnO$_2$ nanocomposite (purple line), the same two mass loss steps were observed. The first one between 70 and 220 °C corresponded to a weight loss of 2.2%. Since this step was associated with the elimination of physically adsorbed water, the reduction in the weight loss compared to pure SnO$_2$ NPs can indicate that RGO prevents water adsorption, which is consistent with FTIR results. In the second mass loss step, the RGO-SnO$_2$ nanocomposite lost more weight than pure SnO$_2$ NPs, corresponding to 6.3%. In addition, the nanocomposite curve was more abrupt from 330 °C to 530 °C. These results suggest that the RGO fraction can be eliminated in this range of temperature.

XPS was carried out to determine the surface chemical composition and the valence state of the corresponding elements (Fig. 5). The survey scan XPS spectra of SnO$_2$ NPs and RGO-SnO$_2$ nanocomposite are shown in Fig. 5a. As it can be seen, only peaks related to Sn, O, and C elements were observed. In the case of the nanocomposite, the peak of Sn 3d was much more intense than C 1s, which means that RGO did not wrap the SnO$_2$ NPs. The relative quantification of the elements provided the values for carbon, tin, and oxygen of 14.6, 45.2, and 40.2%, respectively, for pure SnO$_2$ NPs. While for the RGO-SnO$_2$ nanocomposite, the quantification was about 23.7, 38.4, and 37.9% for carbon, tin, and oxygen, respectively. The increase in carbon quantification was due to the RGO content in the nanocomposite. The high-resolution spectra of Sn, O, and C are shown in Fig. 5b–d, respectively. The Sn 3d spectra revealed two peaks with good symmetry at 495.1 eV and 486.7 eV, corresponding to Sn 3d$_{3/2}$ and Sn 3d$_{5/2}$, respectively. The splitting between the two peaks was 8.4 eV, indicating the single oxidation valence state of Sn^{4+} [51]. The high-resolution spectra of O 1s (Fig. 5c) were asymmetric and consisted of two peaks with binding energies of ~531.9 eV and ~530.6 eV. The peak at 531.9 eV could be assigned to adsorbed oxygen (O$_x^-$) species on SnO$_2$ surface and the peak at 530.6 eV was attributed to lattice oxygen of SnO$_2$ (O$_{latt}$) [52]. The C 1s spectra (Fig. 5d) showed three components: C−C (284.8 eV), C−OH (286.3 eV), and O−C=O (288.7 eV), which are typical of adventitious carbon contamination, given that they were also present in the spectrum of pure SnO$_2$. However, similar components of C 1s are also reported as graphene contribution [17,22,53], indicating that in the RGO-SnO$_2$ nanocomposite

Sherrer's equation was estimated to be 5.8 nm for all samples, which is in good agreement with TEM results.

Raman spectroscopy was performed to confirm the presence of the reduced form of GO in the nanocomposite (Fig. 4b). The RGO-SnO$_2$ nanocomposite showed two characteristic peaks at 1323 cm^{-1} and 1602 cm^{-1} corresponding to the D and G bands, respectively. The D band is related to the structural defects and partially disordered structures of sp^2 domains [41,42], and the G band is attributed to the first order scattering of the E$_{2g}$ phonon from sp^2 carbon atoms [43]. In comparison with the Raman spectrum of GO (Fig. S2), it can be seen that the intensity ratio I$_D$/I$_G$ increased from 1.24 for GO to 1.33 for RGO-SnO$_2$ nanocomposite. Such increase in I$_D$/I$_G$ suggests that GO has been greatly reduced to RGO in the nanocomposites during the MAS synthesis [44]. Furthermore, peaks related to rutile structure of SnO$_2$ were noticed. The peaks at 626 cm^{-1} and 770 cm^{-1} are attributed to the A$_{1g}$ and B$_{2g}$ vibrational modes, which are associated with the expansion and contraction vibration mode of Sn-O bonds [45]. Moreover, the peaks at 352 cm^{-1} and 572 cm^{-1} are not usual in Raman spectra of bulk structures [45], because they are related to the nano size of the granule, which results in local lattice disorder and oxygen vacancies, producing such new Raman peaks [11,46].
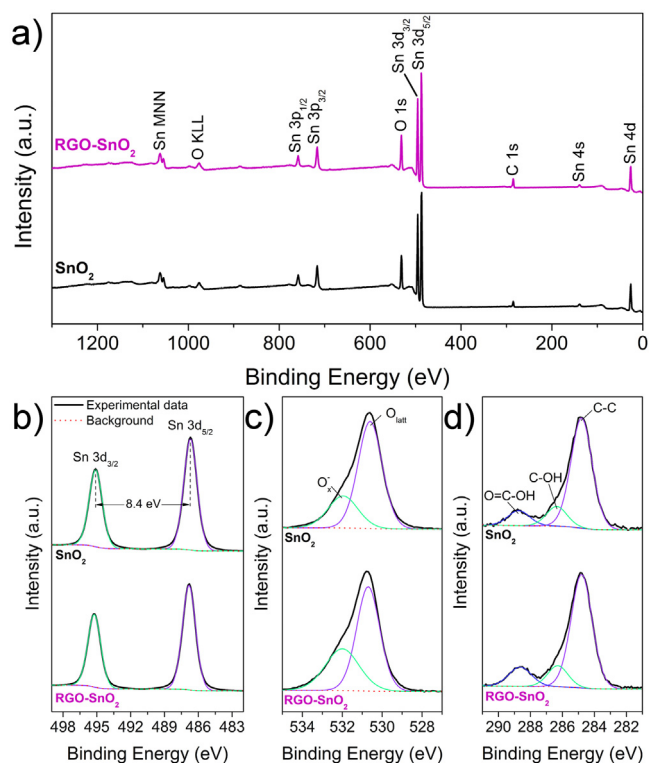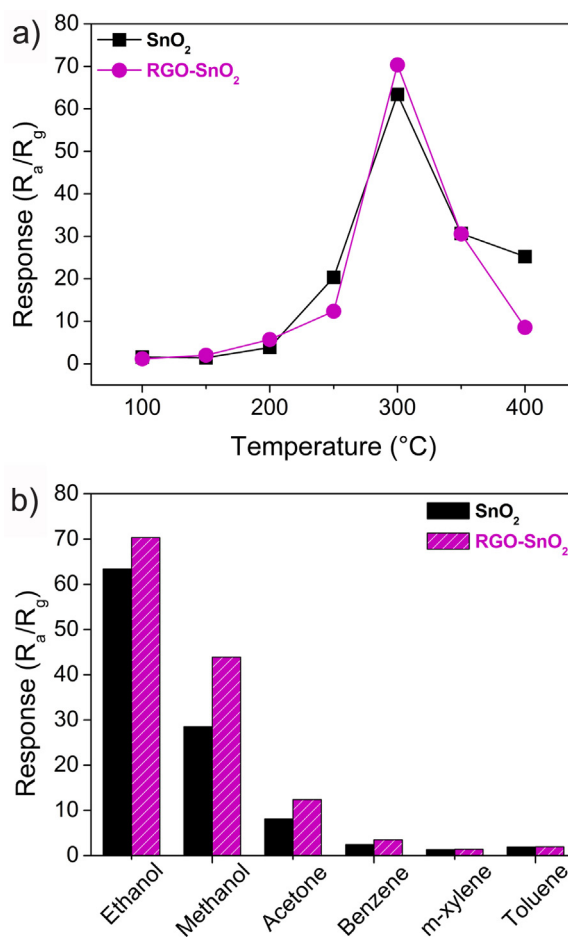
The specific surface area determined by BET method of hollow SnO$_2$ NPs was estimated to be 88 m^2 g^{-1}. Such relative high specific surface area probably arises from the hollow structure of SnO$_2$ NPs.

Fig. 5. (a) Survey-scan XPS spectra of SnO_2 and $RGO-SnO_2$. High-resolution XPS spectra of (b) Sn 3d; (c) O 1s; (d) C 1s, of SnO_2, and $RGO-SnO_2$.

spectrum, RGO contributed at such peaks. The RGO contribution could be confirmed by the increase in carbon value in the relative quantification.

3.3. VOCs sensing performance

To verify the optimal operating temperature of the sensors, the response toward 100 ppm of ethanol was evaluated as a function of the operating temperature (100–400 °C), as shown in Fig. 6a. As it can be seen, the response of the sensors based on SnO_2 NPs and $RGO-SnO_2$ increased with the temperature increasing until 300 °C and decreased when the temperature was above 300 °C. The maximum responses at 300 °C of the sensors based on pure SnO_2 and $RGO-SnO_2$ nanocomposite were 63.4 and 70.4, respectively. The RGO content showed to improve the ethanol sensing response of SnO_2. Hereafter, the subsequent gas sensing studies were carried out at the optimum operating temperature of 300 °C.
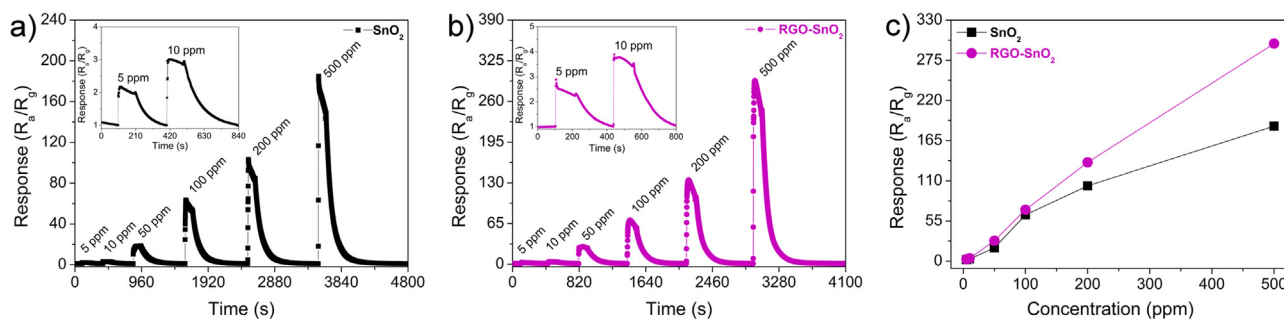
Afterward, the sensibility of the sensors toward different gases at the optimum temperature was evaluated, as shown in Fig. 6b.
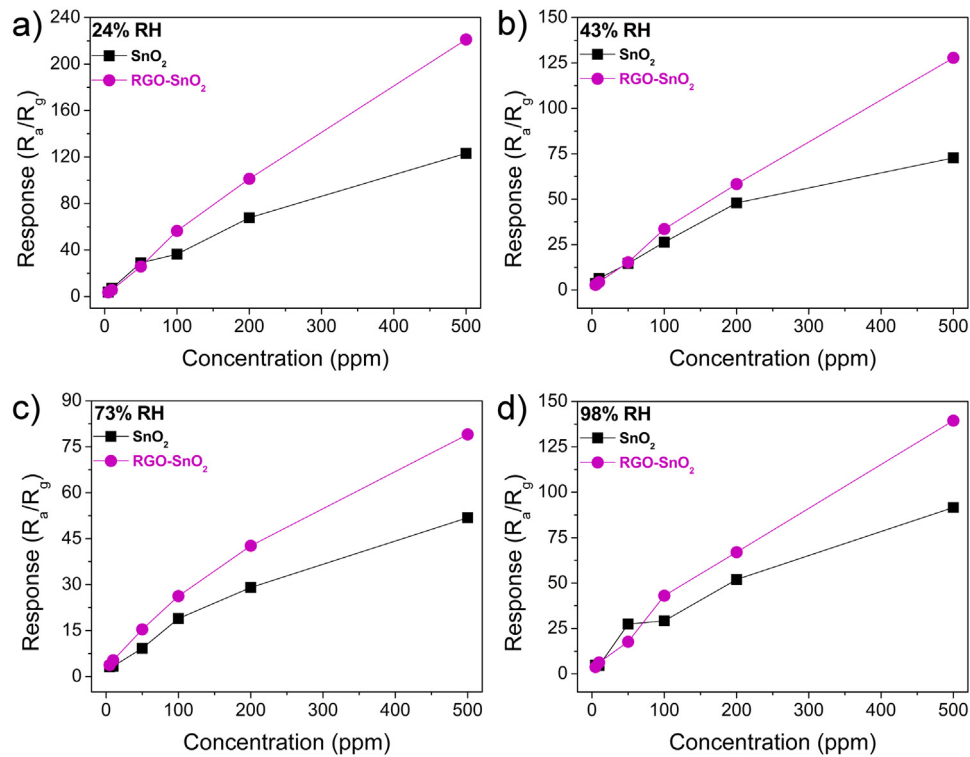

Fig. 6. (a) Response of the sensors toward 100 ppm of ethanol in function of the operating temperature; (b) responses of pure SnO_2 and $RGO-SnO_2$ nanocomposite to 100 ppm of different VOCs at 300 °C.

Both sensors showed better selectivity to ethanol than to the other gases, such as acetone, methanol, benzene, m-xylene, and toluene. For pure SnO_2, the response toward ethanol was about 2.2–48.8 times higher in comparison with other gases, whereas the ratio was 1.6–50.3 for $RGO-SnO_2$ nanocomposite.

The dynamic responses of the sensors to different concentrations of ethanol (5–500 ppm) at 300 °C are shown in Fig. 7a–b. The responses of the sensors increased with increasing ethanol concentration from 5 to 500 ppm, and the sensors exhibited a great capability of reversibility. As exhibited in the insets of Fig. 7a–b, the responses toward 5 and 10 ppm of ethanol are very similar for both sensors. Fig. 7c displays the responses of SnO_2 and RGO-

Fig. 7. Dynamic responses to ethanol in the range of concentration of 5–500 ppm of the sensors based on (a) pure SnO_2; (b) $RGO-SnO_2$ nanocomposite. The insets show the amplification of the responses to 5 and 10 ppm. (c) Responses of pure SnO_2 and $RGO-SnO_2$ nanocomposite as a function of ethanol concentration in dry air at 300 °C.
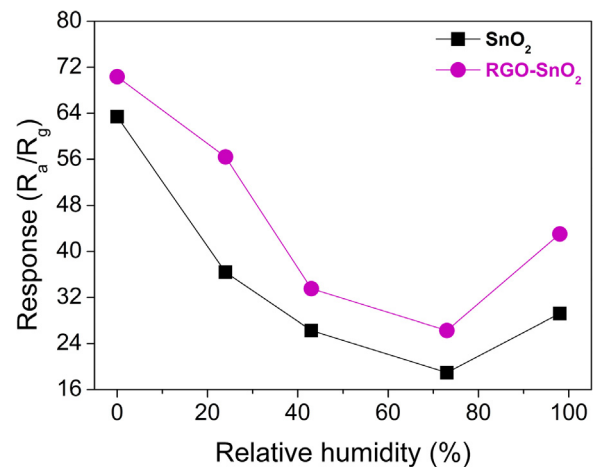
Fig. 8. Responses of pure SnO_2 NPs, and RGO-SnO_2 nanocomposite as a function of ethanol concentration at 300 °C under wet atmosphere with RH of (a) 24%, (b) 43%, (c) 73%, and (d) 98%.

SnO_2 nanocomposite as a function of ethanol concentration. The response of the sensor RGO-SnO_2 was higher than that of pure SnO_2. The responses to 5–500 ppm changed from 2.2 to 184.7, and from 2.7 to 297.8 for the sensors based on SnO_2 and RGO-SnO_2, respectively.

In order to evaluate the humidity effect, the ethanol sensing tests were conducted under a RH of 24, 43, 73, and 98%. Fig. 8a–c, and d display the responses of pure SnO_2 NPs and RGO-SnO_2 nanocomposite as a function of ethanol concentration under a RH of 24%, 43%, 73%, and 98%, respectively. Under all different RH, the sensor based on RGO-SnO_2 nanocomposite showed a superior response to ethanol than SnO_2 NPs. However, the ethanol performance decreased under all wet conditions in comparison with dry air. When the RH was 24%, the responses to 5–500 ppm of ethanol changed from 3.8 to 123.2, and 3.5–221.2 for the sensors based on SnO_2, and RGO-SnO_2, respectively. Under a RH of 43%, the response to 5–500 ppm altered from 3.7 to 72.7, and 2.8–127.8 for pure SnO_2, and RGO-SnO_2, respectively. Increasing the RH to 73%, the sensor signal to the range of 5–500 ppm of ethanol raised from 3.1 to 51.8, and 3.7–79.0 for pure SnO_2, and RGO-SnO_2, respectively. Achieving the highest RH of 98%, the response range observed was 4.8–91.6, and 3.7–139.4 for the sensors based on pure SnO_2 NPs, and RGO-SnO_2.

Fig. 9 sums up the response toward 100 ppm of ethanol under different RH. It is clear that the responses decreased as increasing the RH in comparison with dry conditions. Under 98% of RH, the response was about 29.2 and 43.0 for the sensors SnO_2, and RGO-SnO_2, which were higher than the values found when RH was 43 and 73% of RH. Moreover, the RGO-SnO_2 nanocomposite demonstrated to be less affected by the humidity presence, showing a lower decrease in ethanol response.

Some ethanol sensing results of SnO_2 based materials from the literature are summarized in Table 1. Our hollow SnO_2 NPs and, especially, RGO-SnO_2 nanocomposite exhibited an excellent ethanol sensing performance even when RH was 98%. The response

Fig. 9. Response of the sensors based on SnO_2 and RGO-SnO_2 nanocomposite to 100 ppm of ethanol as a function of the relative humidity at 300 °C.
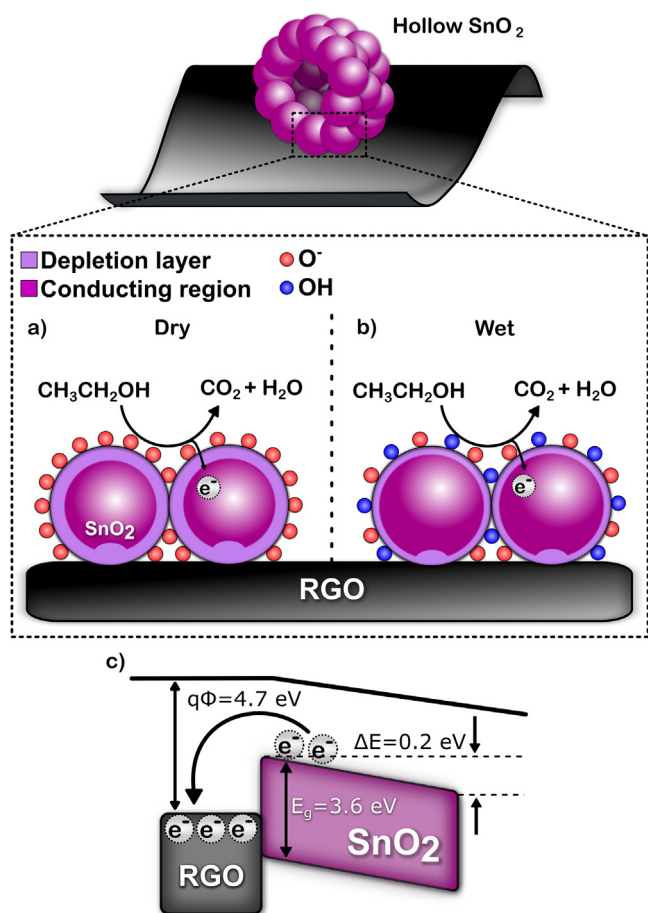
time under dry air and a RH of 98% changed from 9 s to 2 s, and from 11 s to 8 s for SnO_2 NPs and RGO-SnO_2, respectively. Such values of response-time are comparable with literature results and demonstrated that wet conditions did not interfere negatively in this sensor parameter.

3.4. Ethanol sensing mechanism

The gas-sensing mechanism is based on the reactions between oxygen adsorbed on SnO_2 surface and the target gas, according to the ionosorption model. After exposure to air, oxygen species are ionosorbed on SnO_2 surface (O_2^-, O^- or O^{2-}) [57] by the transference of electrons from the conduction band (CB), creating a depletion layer close to the particle surface. Once the sensor is
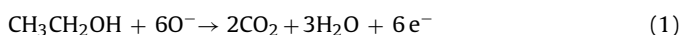
Table 1
Comparison of the gas sensing performance of SnO₂ based sensors toward ethanol.

Structures	Working temperature (°C)	Concentration (ppm)	Gas response (R_{air}/R_{gas})	Response time (s)	Relative humidity	Ref.
SnO₂ nanowires	360	100	31	1–10	Dry air	[54]
SnO₂ nanotubes	300	200	16.7	7	30%	[55]
SnO₂ nanoflowers	300	100	47.29	10	Dry air	[56]
SnO₂@ZnO nanospheres	270	50	7.5	1.2	33%	[30]
Hierarchical SnO₂ nanostructures	Not mentioned	100	44.7	1	Dry air	[11]
SnO₂ nanoflower	240	200	62.2	10	Dry air	[10]
Hollow SnO₂ NPs	300	100	63.4	9	Dry air	This work
Hollow SnO₂ NPs	300	100	29.2	2	98%	This work
RGO-SnO₂ nanocomposite	300	100	70.4	11	Dry air	This work
RGO-SnO₂ nanocomposite	300	100	43.0	8	98%	This work

Fig. 10. Schematic illustration of ethanol sensing mechanism of RGO-SnO₂ nanocomposite in dry air and humid atmosphere. (a) In dry air, SnO₂ nanoparticles, that compose the hollow spherical structure, contain ionosorbed O⁻ species that react with ethanol; (b) in humid conditions occurs the formation of terminal hydroxyl on SnO₂ surface by water poisoning, which also reduces the depletion layer; (c) the RGO/SnO₂ heterojunction in dry air promotes electron transfer from RGO to SnO₂ causing a band bending. As a result, the depletion region is increased as well as the response toward ethanol.

exposed to a reducing gas, such as ethanol, a reaction between the oxygen species and the gas occurs, removing these oxygen species and releasing the electrons back to SnO₂ CB, leading to a decrease in the depletion layer along with a resistance decrease. The dominant ionosorbed oxygen species can be determined by the gas absorption model of semiconductors, see Fig. S5. For all the sensors, the dominant species were found to be O⁻. Thus, the reaction between ethanol and O⁻ species can be represented as Eq. (1):

$$CH_3CH_2OH + 6O^- \rightarrow 2CO_2 + 3H_2O + 6e^- \qquad (1)$$

The sensing mechanism is shown in Fig. 10. Since SnO₂ NPs and RGO-SnO₂ nanocomposite present a high specific surface area, they contain an enhanced quantity of ionosorbed oxygen species on the surface, which also increases the depletion layer of SnO₂. Moreover, the hollow structure and nano size of SnO₂ particles allow an efficient diffusion of oxygen and test gas (ethanol) to active sites. All these parameters helped in the high sensitivity of the materials toward ethanol, even for the pure hollow SnO₂ NPs.

In the nanocomposite, the conduction path is mainly through SnO₂ NPs due to the small amount of RGO [58], however RGO affects the electrical transport properties of SnO₂ (Fig. 10a). Once RGO and SnO₂ are in contact, electrons are transferred from SnO₂ NPs to RGO due to the difference between their work function, which are 4.5 eV for SnO₂ and 4.7 eV for RGO [51,59], resulting in a band-bending of 0.2 eV at the RGO/SnO₂ heterojunction (Fig. 10c). Thus, RGO reduces the quantity of electrons on SnO₂ surface (increases the electron depletion layer), leading to an enhanced resistance changes after the exposure to ethanol [2,59].

Under humid atmosphere, the decrease in ethanol responses can be attributed to the water vapor poisoning. Studies have shown that under conditions, water reacts with ionosorbed oxygen species on SnO₂ surface, resulting in the formation of terminal hydroxyl groups, according to the following reaction (Eq. (2)) [60,61]:

$$H_2O_{(g)} + O^- + 2Sn + \rightleftharpoons 2(Sn\text{-}OH) + e^- \qquad (2)$$
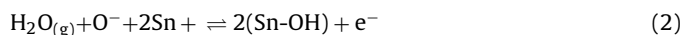
In the equation, H₂O represents a water molecule from the humid atmosphere, O⁻ is the predominant ionosorbed oxygen species in our studies, Sn is the Sn ion on SnO₂ surface, which from our XPS results demonstrated to be in the single form of Sn⁴⁺, Sn-OH is the resulting terminal hydroxyl groups, and e⁻ is the released electron from the adsorbed oxygen to CB. Therefore, the formation of terminal hydroxyl groups leads to a reduction in the depletion layer of SnO₂ NPs and, consequently, to a decrease in the sensors resistance (Fig. 10b). Moreover, the ethanol molecules compete with water vapor for ionosorbed oxygen species on SnO₂ surface [62]. Both consequences of humidity presence contribute to the lower responses to ethanol under wet conditions.

However, our results demonstrated that the RGO content helped to suppress the adverse effect of humidity. This effect could be explained by the heterojunction RGO/SnO₂, which promotes an increased depletion layer in comparison with pure SnO₂. Thus, the RGO-SnO₂ nanocomposite continued showing an enhanced ethanol response under humid conditions. Moreover, RGO shows a low humidity sensitivity [38] which associated with its hydrophobicity can achieve a lower humidity interfering effect than pure SnO₂ NPs [63]. Therefore, the electrons transfer from SnO₂ to RGO continues effectively under wet atmosphere, and the ethanol sensing performance of RGO-SnO₂ nanocomposite is preserved.

4. Conclusions

In summary, RGO-SnO$_2$ nanocomposite was successfully prepared by a one-step microwave-assisted solvothermal synthesis. In the gas sensing studies, the RGO-SnO$_2$ nanocomposite exhibited an enhanced ethanol sensing performance compared to pure hollow SnO$_2$ NPs in dry and humid atmosphere. When RH was 98%, the RGO-SnO$_2$ nanocomposite showed a sensing response of 43.0–100 ppm of ethanol with a response time of 8 s.

Morphological and structural characterizations confirmed that the applied synthetic method led to the formation of RGO-SnO$_2$ nanocomposite with suitably well-dispersed crystalline SnO$_2$ structures on RGO sheets (the graphene oxide reduction occurred simultaneously to the SnO$_2$ NPs formation). The size and hollow structure of SnO$_2$ NPs, which provided an efficient diffusion of ethanol molecules, and the RGO content were responsible for the superior ethanol sensing performance. The RGO/SnO$_2$ heterojunction increased the depletion region and as well as the response toward ethanol. Moreover, RGO played a major role to mitigate the negative impact of humidity on ethanol sensing performance.

Hence, the use of well-designed RGO-SnO$_2$ nanocomposite is a promising approach for real-world applications of chemiresistive-type sensors where humidity is a major interfering.

Acknowledgments

Appendix A. Supplementary data

Supplementary data associated with this article can be found, in the online version, at http://dx.doi.org/10.1016/j.snb.2017.01.015.

References

[1] D. Jiang, W. Wei, F. Li, Y. Li, C. Liu, D. Sun, C. Feng, S. Ruan, Xylene gas sensor based on α-MoO$_3$/α-Fe$_2$O$_3$ heterostructure with high response and low operating temperature, RSC Adv. 5 (2015) 39442–39448, http://dx.doi.org/10.1039/C5RA05661F.

[2] S.-J. Choi, B.-H. Jang, S.-J. Lee, B.K. Min, A. Rothschild, I.-D. Kim, Selective detection of acetone and hydrogen sulfide for the diagnosis of diabetes and halitosis using SnO$_2$ nanofibers functionalized with reduced graphene oxide nanosheets, ACS Appl. Mater. Interfaces 6 (2014) 2588–2597, http://dx.doi.org/10.1021/am405088q.

[3] C. Dong, X. Liu, X. Xiao, G. Chen, Y. Wang, I. Djerdj, Combustion synthesis of porous Pt-functionalized SnO$_2$ sheets for isopropanol gas detection with a significant enhancement in response, J. Mater. Chem. A 2 (2014) 20089–20095, http://dx.doi.org/10.1039/C4TA04251D.

[4] C. Wang, X. Cui, J. Liu, X. Zhou, X. Cheng, P. Sun, X. Hu, X. Li, J. Zheng, G. Lu, Design of superior ethanol gas sensor based on Al-doped NiO nanorod-flowers, ACS Sens. 1 (2015) 131–136, http://dx.doi.org/10.1021/acssensors.5b00123.

[5] H. Yu, S. Wang, C. Xiao, B. Xiao, P. Wang, Z. Li, M. Zhang, Enhanced acetone gas sensing properties by aurelia-like SnO$_2$ micro-nanostructures, CrystEngComm 17 (2015) 4316–4324, http://dx.doi.org/10.1039/C5CE00448A.

[6] Y. Zeng, Y. Wang, L. Qiao, Y. Bing, B. Zou, W. Zheng, Synthesis and the improved sensing properties of hierarchical SnO$_2$ hollow nanosheets with mesoporous and multilayered interiors, Sens. Actuators B 222 (2016) 354–361, http://dx.doi.org/10.1016/j.snb.2015.08.068.

[7] C. Zhang, J. Wang, R. Hu, Q. Qiao, X. Li, Synthesis and gas sensing properties of porous hierarchical SnO$_2$ by grapefruit exocarp biotemplate, Sens. Actuators B 222 (2016) 1134–1143, http://dx.doi.org/10.1016/j.snb.2015.08.016.

[8] J. Huang, L. Wang, C. Gu, Z. Wang, Y. Sun, J.-J. Shim, Preparation of porous SnO$_2$ microcubes and their enhanced gas-sensing property, Sens. Actuators B 207 (2015) 782–790, http://dx.doi.org/10.1016/j.snb.2014.10.128.

[9] K. Suematsu, Y. Shin, Z. Hua, K. Yoshida, M. Yuasa, T. Kida, K. Shimanoe, Nanoparticle cluster gas sensor: controlled clustering of SnO$_2$ nanoparticles for highly sensitive toluene detection, ACS Appl. Mater. Interfaces 6 (2014) 5319–5326, http://dx.doi.org/10.1021/am500944a.

[10] T. Li, W. Zeng, H. Long, Z. Wang, Nanosheet-assembled hierarchical SnO$_2$ nanostructures for efficient gas-sensing applications, Sens. Actuators B 231 (2016) 120–128, http://dx.doi.org/10.1016/j.snb.2016.03.003.

[11] Y. Liu, Y. Jiao, Z. Zhang, F. Qu, A. Umar, X. Wu, Hierarchical SnO$_2$ nanostructures made of intermingled ultrathin nanosheets for environmental remediation, smart gas sensor, and supercapacitor applications, ACS Appl. Mater. Interfaces 6 (2014) 2174–2184, http://dx.doi.org/10.1021/am405301v.

[12] J. Wang, Y. Xu, W. Xu, M. Zhang, X. Chen, Simplified preparation of SnO$_2$ inverse opal for methanol gas sensing performance, Microporous Mesoporous Mater. 208 (2015) 93–97, http://dx.doi.org/10.1016/j.micromeso.2015.01.038.

[13] D. Pradhan, A.K. Nayak, R. Ghosh, S. Santra, P.K. Guha, Hierarchical nanostructured WO$_3$-SnO$_2$ for selective sensing of volatile organic compounds, Nanoscale (2015) 12460–12473, http://dx.doi.org/10.1039/C5NR02571K.

[14] T. Wang, Z. Huang, Z. Yu, B. Wang, H. Wang, P. Sun, H. Suo, Y. Gao, Y. Sun, T. Li, G. Lu, Low operating temperature toluene sensor based on novel α-Fe$_2$O$_3$/SnO$_2$ heterostructure nanowire arrays, RSC Adv. 6 (2016) 52604–52610, http://dx.doi.org/10.1039/C6RA05313K.

[15] Y.V. Kaneti, J. Yue, J. Moriceau, C. Chen, M. Liu, Y. Yuan, X. Jiang, A. Yu, Experimental and theoretical studies on noble metal decorated tin oxide flower-like nanorods with high ethanol sensing performance, Sens. Actuators B 219 (2015) 83–93, http://dx.doi.org/10.1016/j.snb.2015.04.136.

[16] C. Liu, Q. Kuang, Z. Xie, L. Zheng, The effect of noble metal (Au, Pd and Pt) nanoparticles on the gas sensing performance of SnO$_2$-based sensors: a case study on the {221} high-index faceted SnO$_2$ octahedra, CrystEngComm 17 (2015) 6308–6313, http://dx.doi.org/10.1039/C5CE01162K.

[17] S. Chen, Y. Qiao, J. Huang, H. Yao, Y. Zhang, Y. Li, J. Du, W. Fan, One-pot synthesis of mesoporous spherical SnO$_2$@graphene for high-sensitivity formaldehyde gas sensors, RSC Adv. 6 (2016) 25198–25202, http://dx.doi.org/10.1039/C6RA00857G.

[18] Z. Song, Z. Wei, B. Wang, Z. Luo, S. Xu, Z. Song, Z. Wei, B. Wang, Z. Luo, S. Xu, W. Zhang, H. Yu, M. Li, Sensitive room-temperature H$_2$S gas sensors employing SnO$_2$ quantum wire/reduced graphene oxide nanocomposites, Chem. Mater. 28 (2016) 1205–1212, http://dx.doi.org/10.1021/acs.chemmater.5b04850.

[19] S. Liu, Z. Wang, Y. Zhang, C. Zhang, T. Zhang, High performance room temperature NO$_2$ sensors based on reduced graphene oxide-multiwalled carbon nanotubes-tin oxide nanoparticles hybrids, Sens. Actuators B 211 (2015) 318–324, http://dx.doi.org/10.1016/j.snb.2015.01.127.

[20] Z. Wang, Y. Zhang, S. Liu, T. Zhang, Preparation of Ag nanoparticles-SnO$_2$ nanoparticles-reduced graphene oxide hybrids and their application for detection of NO$_2$ at room temperature, Sens. Actuators B 222 (2016) 893–903, http://dx.doi.org/10.1016/j.snb.2015.09.027.

[21] Z. Wang, C. Zhao, T. Han, Y. Zhang, S. Liu, T. Fei, G. Lu, T. Zhang, High-performance reduced graphene oxide-based room-temperature NO$_2$ sensors: a combined surface modification of SnO$_2$ nanoparticles and nitrogen doping approach, Sens. Actuators B 242 (2017) 269–279, http://dx.doi.org/10.1016/j.snb.2016.10.101.

[22] H. Zhang, J. Feng, T. Fei, S. Liu, T. Zhang, SnO$_2$ nanoparticles-reduced graphene oxide nanocomposites for NO$_2$ sensing at low operating temperature, Sens. Actuators B 190 (2014) 472–478, http://dx.doi.org/10.1016/j.snb.2013.08.067.

[23] G. Lu, S. Park, K. Yu, R.S. Ruoff, L.E. Ocola, D. Rosenmann, J. Chen, Toward practical gas sensing with highly reduced graphene oxide: a new signal processing method to circumvent run-to-run and device-to-device variations, ACS Nano 5 (2011) 1154–1164, http://dx.doi.org/10.1021/nn102803q.

[24] R. Ghosh, A.K. Nayak, S. Santra, D. Pradhan, P.K. Guha, Enhanced ammonia sensing at room temperature with reduced graphene oxide/tin oxide hybrid films, RSC Adv. 5 (2015) 50165–50173, http://dx.doi.org/10.1039/C5RA06696D.

[25] R.G. Pavelko, H. Daly, C. Hardacre, A.A. Vasiliev, E. Llobet, Interaction of water, hydrogen and their mixtures with SnO$_2$ based materials: the role of surface hydroxyl groups in detection mechanisms, Phys Chem. Chem. Phys. 12 (2010) 2639–2647, http://dx.doi.org/10.1039/b921665k.

[26] N. Kahn, O. Lavie, M. Paz, Y. Segev, H. Haick, Dynamic nanoparticle-based flexible sensors: diagnosis of ovarian carcinoma from exhaled breath, Nano Lett. 15 (2015) 7023–7028, http://dx.doi.org/10.1021/acs.nanolett.5b03052.

[27] S.-J. Choi, S. Chattopadhyay, J.J. Kim, S.-J. Kim, H.L. Tuller, G.C. Rutledge, I.-D. Kim, Coaxial electrospinning of WO$_3$ nanotubes functionalized with bio-inspired Pd catalysts and their superior hydrogen sensing performance, Nanoscale 8 (2016) 9159–9166, http://dx.doi.org/10.1039/C5NR06611E.

[28] N. Ma, K. Suematsu, M. Yuasa, T. Kida, K. Shimanoe, Effect of water vapor on Pd-loaded SnO$_2$ nanoparticles gas sensor, ACS Appl. Mater. Interfaces 7 (2015) 5863–5869, http://dx.doi.org/10.1021/am509082w.

[29] H. Tian, H. Fan, M. Li, L. Ma, Zeolitic Imidazolate framework coated ZnO nanorods as molecular sieving to improve selectivity of formaldehyde gas sensor, ACS Sens. 1 (2016) 243–250, http://dx.doi.org/10.1021/acssensors.5b00236.

[30] R. Zhang, T. Zhou, L. Wang, Z. Lou, J. Deng, T. Zhang, The synthesis and fast ethanol sensing properties of core–shell SnO$_2$@ZnO composite nanospheres

using carbon spheres as templates, New J. Chem. 40 (2016) 6796–6802, http://dx.doi.org/10.1039/C6NJ00365F.

[31] A. Tricoli, M. Righettoni, S.E. Pratsinis, Minimal cross-sensitivity to humidity during ethanol detection by SnO_2-TiO_2 solid solutions, Nanotechnology 20 (2009) 315502, http://dx.doi.org/10.1088/0957-4484/20/31/315502.

[32] K. Suematsu, M. Sasaki, N. Ma, M. Yuasa, K. Shimanoe, Antimony-doped tin dioxide gas sensors exhibiting high stability in the sensitivity to humidity changes, ACS Sens. 1 (2016) 913–920, http://dx.doi.org/10.1021/acssensors.6b00323.

[33] N. Ma, K. Suematsu, M. Yuasa, K. Shimanoe, Pd size effect on the gas sensing properties of Pd-loaded SnO_2 in humid atmosphere, ACS Appl. Mater. Interfaces 7 (2015) 15618–15625, http://dx.doi.org/10.1021/acsami.5b04380.

[34] T.M. Perfecto, C.A. Zito, D.P. Volanti, Room-temperature volatile organic compounds sensing based on $WO_3 \cdot 0.33H_2O$ hexagonal-WO_3, and their reduced graphene oxide composites, RSC Adv. 6 (2016) 105171–105179, http://dx.doi.org/10.1039/C6RA16892B.

[35] W.S. Hummers, R.E. Offeman, Preparation of graphitic oxide, J. Am. Chem. Soc. 80 (1958), http://dx.doi.org/10.1021/ja01539a017, 1339–1339.

[36] W. Wu, S. Zhang, J. Zhou, X. Xiao, F. Ren, C. Jiang, Controlled synthesis of monodisperse sub-100 nm hollow SnO_2 nanospheres: a template-and surfactant-free solution-phase route, the growth mechanism, optical properties, and application as a photocatalyst, Chem.-A Eur. J. 17 (2011) 9708–9719, http://dx.doi.org/10.1002/chem.201100694.

[37] E.L. Silva, J.A. Varela, D.K.A. Almeida, D.P. Volanti, Aided device for hydrothermal synthesis of nanostructured oxides, particularly obtaining particles of metal oxides, comprises container, in which hydrothermal reaction takes place, and lid for container, BR200815393-A2, 2010.

[38] Z. Wang, Y. Xiao, X. Cui, P. Cheng, B. Wang, Y. Gao, X. Li, T. Yang, T. Zhang, G. Lu, Humidity-sensing properties of urchinlike CuO nanostructures modified by reduced graphene oxide, ACS Appl. Mater. Interfaces 6 (2014) 3888–3895, http://dx.doi.org/10.1021/am404858z.

[39] B.L. Caetano, F. Meneau, C.V. Santilli, S.H. Pulcinelli, M. Magnani, V. Briois, Mechanisms of SnO_2 nanoparticles formation and growth in acid ethanol solution derived from SAXS and combined raman-XAS time-resolved studies, Chem. Mater. 26 (2014) 6777–6785, http://dx.doi.org/10.1021/cm5032688.

[40] J.-P. Jolivet, M. Henry, J. Livage, Metal Oxide Chemistry and Synthesis: from Solution to Solid State, John Wiley, 2000.

[41] P.G. Su, L.Y. Yang, NH_3 gas sensor based on Pd/SnO_2/RGO ternary composite operated at room-temperature, Sens. Actuators B 223 (2016) 202–208, http://dx.doi.org/10.1016/j.snb.2015.09.091.

[42] S. Some, Y. Kim, Y. Yoon, H. Yoo, S. Lee, Y. Park, H. Lee, High-quality reduced graphene oxide by a dual-function chemical reduction and healing process, Sci. Rep. 3 (2013) 1929, http://dx.doi.org/10.1038/srep01929.

[43] P. Khanra, T. Kuila, N.H. Kim, S.H. Bae, D. Yu, J.H. Lee, Simultaneous bio-functionalization and reduction of graphene oxide by baker's yeast, Chem. Eng. J. 183 (2012) 526–533, http://dx.doi.org/10.1016/j.cej.2011.12.075.

[44] H. Meng, W. Yang, K. Ding, L. Feng, Y. Guan, Cu_2O nanorods modified by reduced graphene oxide for NH_3 sensing at room temperature, J. Mater. Chem. A 3 (2015) 1174–1181, http://dx.doi.org/10.1039/C4TA06024E.

[45] G. Cheng, J. Wang, X. Liu, K. Huang, Self-assembly synthesis of single-crystalline tin oxide nanostructures by a poly(acrylic acid)-assisted solvothermal process, J. Phys. Chem. B 110 (2006) 16208–16211, http://dx.doi.org/10.1021/jp061935q.

[46] A. Birkel, F. Reuter, D. Koll, S. Frank, R. Branscheid, M. Panthöfer, E. Rentschler, W. Tremel, The interplay of crystallization kinetics and morphology during the formation of SnO_2 nanorods: snapshots of the crystallization from fast microwave reactions, CrystEngComm 13 (2011) 2487, http://dx.doi.org/10.1039/c0ce00573h.

[47] P. Gurunathan, P.M. Ette, K. Ramesha, Synthesis of hierarchically porous SnO_2 microspheres and performance evaluation as Li-ion battery anode by using different binders, ACS Appl. Mater. Interfaces 6 (2014) 16556–16564, http://dx.doi.org/10.1021/am502852x.

[48] J. Jouhannaud, J. Rossignol, D. Stuerga, Rapid synthesis of tin (IV) oxide nanoparticles by microwave induced thermohydrolysis, J. Solid State Chem. 181 (2008) 1439–1444, http://dx.doi.org/10.1016/j.jssc.2008.02.040.

[49] Z. Chen, C.-H. Shek, C.M. Lawrence Wu, Insights from investigations of tin dioxide and its composites: electron-beam irradiation, fractal assessment, and mechanism, Nanoscale 7 (2015) 15532–15552, http://dx.doi.org/10.1039/C5NR04255JK.

[50] K.C. Song, Y. Kang, Preparation of high surface area tin oxide powders by a homogeneous precipitation method, Mater. Lett. 42 (2000) 283–289, http://dx.doi.org/10.1016/S0167-577X(99)00199-8.

[51] B.H. Jang, O. Landau, S.J. Choi, J. Shin, A. Rothschild, I.D. Kim, Selectivity enhancement of SnO_2 nanofiber gas sensors by functionalization with Pt

nanocatalysts and manipulation of the operation temperature, Sens. Actuators B 188 (2013) 156–168, http://dx.doi.org/10.1016/j.snb.2013.07.011.

[52] X. Liu, N. Chen, B. Han, X. Xiao, G. Chen, I. Djerdj, Y. Wang, Nanoparticle cluster gas sensor: pt activated SnO_2 nanoparticles for NH_3 detection with ultrahigh sensitivity, Nanoscale 7 (2015) 14872–14880, http://dx.doi.org/10.1039/C5NR03585F.

[53] C. Zhu, S. Zhu, K. Zhang, Z. Hui, H. Pan, Z. Chen, Y. Li, D. Zhang, D.W. Wang, Confined SnO2 quantum-dot clusters in graphene sheets as high-performance anodes for lithium-ion batteries, Sci. Rep. 6 (2016) 25829, http://dx.doi.org/10.1038/srep25829.

[54] S. Phadungdhitidhada, S. Thanasanvorakun, P. Mangkorntong, S. Choopun, N. Mangkorntong, D. Wongratanaphisan, SnO_2 nanowires mixed nanodendrites for high ethanol sensor response, Curr. Appl. Phys. 11 (2011) 1368–1373, http://dx.doi.org/10.1016/j.cap.2011.04.007.

[55] J. Zhang, J. Guo, H. Xu, B. Cao, Reactive-template fabrication of porous SnO_2 nanotubes and their remarkable gas-sensing performance, ACS Appl. Mater. Interfaces 5 (2013) 7893–7898, http://dx.doi.org/10.1021/am4019884.

[56] X. Yu, W. Zeng, Fabrication and gas-sensing performance of nanorod-assembled SnO_2 nanostructures, J. Mater. Sci. Mater. Electron. 27 (2016) 1–6, http://dx.doi.org/10.1007/s10854-016-4721-0.

[57] A. Gurlo, Interplay between O_2 and SnO_2: oxygen ionosorption and spectroscopic evidence for adsorbed oxygen, ChemPhysChem 7 (2006) 2041–2052, http://dx.doi.org/10.1002/cphc.200600292.

[58] N. Tammanoon, A. Wisitsoraat, C. Sriprachuabwong, D. Phokharatkul, A. Tuantranont, S. Phanichphant, C. Liewhiran, Ultrasensitive NO_2 sensor based on ohmic metal-semiconductor interfaces of electrolytically exfoliated graphene/flame-spray-made SnO_2 nanoparticles composite operating at low temperatures, ACS Appl. Mater. Interfaces 7 (2015) 24338–24352, http://dx.doi.org/10.1021/acsami.5b09067.

[59] S.J. Choi, F. Fuchs, R. Demadrille, B. Grévin, B.H. Jang, S.J. Lee, J.H. Lee, H.L. Tuller, I.D. Kim, Fast responding exhaled-breath sensors using WO_3 hemitubes functionalized by graphene-based electronic sensitizers for diagnosis of diseases, ACS Appl. Mater. Interfaces 6 (2014) 9061–9070, http://dx.doi.org/10.1021/am501394r.

[60] K. Großmann, S. Wicker, U. Weimar, N. Barsan, Impact of Pt additives on the surface reactions between SnO_2, water vapour CO and H_2; an operando investigation, Phys. Chem. Chem. Phys. 15 (2013) 19151–19158, http://dx.doi.org/10.1039/c3cp52782d.

[61] D. Koziej, N. Bârsan, U. Weimar, J. Szuber, K. Shimanoe, N. Yamazoe, Water—oxygen interplay on tin dioxide surface: implication on gas sensing, Chem. Phys. Lett. 410 (2005) 321–323, http://dx.doi.org/10.1016/j.cplett.2005.05.107.

[62] M. Hübner, C.E. Simion, A. Tomescu-Stănoiu, S. Pokhrel, N. Bârsan, U. Weimar, Influence of humidity on CO sensing with p-type CuO thick film gas sensors, Sens. Actuators B 153 (2011) 347–353, http://dx.doi.org/10.1016/j.snb.2010.10.046.

[63] I. Sasaki, N. Minami, A. Karthigeyan, K. Iakoubovskii, Optimization and evaluation of networked single-wall carbon nanotubes as a NO_2 gas sensing material, Analyst 134 (2009) 325–330, http://dx.doi.org/10.1039/b813073f.

Biographies

Cecilia de Almeida Zito is a M.Sc. student in Universidade Estadual Paulista. Currently, she is working on the synthesis of materials based on graphene and semiconductors and their application as volatile organic compounds sensors.

Tarcísio Micheli Perfecto is a M.Sc. student in Universidade Estadual Paulista. His current research work involves the application of semiconductors and graphene-based materials as gas sensors at room temperature.

Diogo Paschoalini Volanti received his degree in chemistry from Federal University of São Carlos (UFSCar) and his PhD in chemistry from São Paulo State University (UNESP) in Brazil. He is a member of the faculty of the Department of Chemistry and Environmental Sciences at UNESP in São José do Rio Preto, where he serves as assistant professor of general and inorganic chemistry and director of the Laboratory of Materials for Sustainability (LabMatSus). Dr. Volanti's current research emphasizes the microwave-assisted hydrothermal synthesis, functional semiconductors nanostructures, gas sensors, graphene, heterogeneous catalysis, photocatalysis, transmission electron microscopy, in situ and operando x-ray absorption spectroscopy.